
Article:
Heath, J.P., Harding, J.H. orcid.org/0000-0001-8429-3151, Sinclair, D.C. orcid.org/0000-0002-8031-7678 et al. (1 more author) (2019) The analysis of impedance spectra for core–shell microstructures : why a multiformalism approach is essential. Advanced Functional Materials, 29 (38). ISSN 1616-301X

https://doi.org/10.1002/adfm.201904036

The analysis of Impedance Spectra for Core-Shell Microstructures: Why a multi-formalism approach is essential

James Heath, John Harding, Derek Sinclair, and Julian Dean*

Dr. J. P. Heath, Prof. J. H. Harding, Prof. D. C. Sinclair, Dr. J. S. Dean
Department of Materials Science & Engineering, University of Sheffield, S1 3JD, United Kingdom
E-mail: j.dean@sheffield.ac.uk

Keywords: Core/Shell Microstructures, Dielectrics, Composite Materials, Simulations, Impedance spectra

The impedance response of a core-shell microstructure with 80% core volume fraction has been simulated using finite element modeling and compared to two equivalent circuits for a wide range of shell permittivity and conductivity values. Different equivalent circuits, corresponding to different variants of the well-known brick layer model, are applicable for different combinations of material properties in the microstructure. When the shell has a similar conductivity or permittivity to the core, adding a parallel pathway increases the accuracy of the fit by ~±10%. When both the conductivity and permittivity values of the core and shell regions are different the series circuit is a better fit. This was confirmed by multi-formalism impedance analysis, which revealed features in the data that were not apparent using a single formalism. Finally, the conductivity and permittivity values for both the shell and core were extracted from the simulated spectra using all formalisms and compared to the original input values. The accuracy of the extracted values often depended on the impedance formalism used. We conclude that impedance spectroscopy data must be analyzed using multiple formalisms when considering core-shell microstructures.

1. Introduction

Core-shell microstructures are used (inter alia) for functional,[1, 2] medical[3] and catalysis[4] applications. The popularity of this microstructure stems from the ability to tune its properties by changing the core and shell phase material properties and their volume ratio. We consider the extraction of material properties from impedance spectroscopy measurements of these core-shell structures. We test the ability of existing strategies (such as the brick layer model[5]) to extract properties by comparing them with direct calculation using finite element modelling and suggest improved strategies.

Impedance spectroscopy is a powerful technique for studying frequency-dependent electrochemical behaviour. The technique is widely used to analyse electroceramics for dielectric,[6] fuel cell[7] and battery applications.[8] Two central issues make the technique challenging for users: the choice of an appropriate equivalent circuit[9] and of formalisms to use for data analysis[10]. Equivalent circuits are combinations of basic circuit components (such as resistors, capacitors or inductors) and constant phase elements that model the electrical behaviour of the system.[11] Unfortunately, different circuits can give the same response.[9] To choose the appropriate circuit requires an understanding of the electrical processes occurring within a sample. Alternative approaches proposed for fitting impedance data include the nano-grain composite model by Kidner et al. [12] and random R-C networks by Almond and Bowen[13].

The impedance ($Z^* = Z' + jZ''$) is a complex number where the real part ($\mathrm{Re}(Z) = Z'$) relates to resistance and the imaginary part ($\mathrm{Im}(Z) = Z''$) relates to the reactive (capacitive) component of the response. Z^* can be transformed into three other complex formalisms: admittance (Y^*), electric modulus (M^*) and complex capacitance (C^*). These transformations weight impedance data differently and the frequency dependence exhibits different sensitivities to electrical components. For example, $Z^*(\omega)$ is sensitive to large resistances

whilst Y*(ω) is more sensitive to small resistances. The relationship between the four formalisms and their sensitivities is detailed in **table S1**. It is common to refer to all four formalisms collectively as the impedance. However, since we have defined the impedance as a specific formalism, distinguishable from Y*, M* and C*, the collective response will be henceforth referred to as the immittance response. From here on, impedance refers only to Z*.

In positive temperature coefficient of resistance (PTCR) $BaTiO_3$ ceramics, there is electrical heterogeneity caused (in part) by a core-shell microstructure where the core is semiconducting and the shell is more resistive. Core-shell microstructures are also employed to improve the temperature stability of the capacitance and the dielectric breakdown strength of $BaTiO_3$-based Multi-Layer Ceramic Capacitors.[14] However, the relative thicknesses of the core and shell regions and their electrical properties are very dependent on the processing conditions. Full characterisation of core-shell microstructures requires knowledge of the core and shell volume fractions. Sometimes it is possible to estimate volume fractions from the experimental capacitance ratios. [15, 16] Finite element modelling[17] (FEM) shows this works reasonably well if the volume of the core is ~80% of the sample and the resistivity of the core is much lower than that of the shell. Therefore we focus on the 80% core volume fraction regime, allowing the assumption of known volume fractions and hence limit the discussion to two issues: “what is the best equivalent circuit?” and “which immittance formalisms should be used to study core-shell microstructures?"

It is common to correct immittance data for the sample dimensions. C* is often corrected in this manner to obtain a complex permittivity (ε*). In this work we present uncorrected resistances and capacitances and then convert them into conductivity and permittivity values (respectively) using the known geometries of the core and shell. Due to the large volume fraction of core (0.8), the extracted conductivity and permittivity values will be similar to those extracted using the sample geometry. However, using the true geometric

factor of the shell will give more accurate values of the conductivity and permittivity than using the geometric factor of the sample.

Since multi-formalism analysis can highlight additional aspects of immittance data, values of the resistance or capacitance could depend on which formalism (or combination of formalisms) is used to extract them. Likewise, if the resistances or capacitances are converted into conductivities or permittivities, these values also depend on the strategy employed. Simulation enables us to define the conductivities and permittivities and therefore test the strategy. We use multi-formalism impedance analysis to extract conductivity and permittivity values from a simple core-shell microstructure. The extracted values are then compared to those put into the model to evaluate the accuracy of different immittance formalisms.

Different disciplines tend to use particular formalisms to analyse immittance data. The dielectrics community favours Z* and C* as these highlight large resistances and capacitances which are often the focus for dielectric materials. Those investigating solid electrolytes favour Y* to highlight the conductive behaviour. It is best practice, however, to use a combination of all four formalisms to characterise the electrical microstructure of a sample. This has been shown experimentally by using combined Z'' and M'' spectroscopic plots to probe electrical heterogeneity in PTCR $BaTiO_3$ ceramics[15] and using all four formalisms to obtain equivalent circuits for oxide-ion conducting doped-lanthanum gallate ceramics. [9] The authors recommend showing the fit of the immittance data over the whole frequency range for all four formalisms.

2. Modeling methodology

We have used a simplified core-shell microstructure (the encased model (see **figure S1 A, B**)) to illustrate the multi-formalism approach. This consists of a cube embedded in a larger cube. The inner cube is the core whilst the remaining volume is the shell. The volume fraction of

the core was kept constant at 0.8 and the whole model had a length of 2 μm. Another microstructural configuration was also considered - the series layer model[18] (SLM, see **figure S1 C, D**). This is one of the simplest models for an electrical composite. Each layer is equivalent to a resistor and capacitor connected in parallel[19] and hence can be solved analytically. The length and area of the SLM are the same as the encased model. The core and shell layers of the SLM have the same area and so their volumes are a function of layer thickness alone. This is chosen to give a core volume fraction of 0.8. Comparing the encased and SLM models, for fixed volume fractions of core and shell material, will show how a change in microstructural configuration affects the electrical response.

Previously, we have shown there was little effect of microstructure on the electrical response of core-shell microstructures when the core volume fraction is ≥ 0.8 (since the conduction through the parallel component of the shell is minimal) [17]. However, that study used core and shell time constants (defined as $\tau_i = R_iC_i = (\varepsilon_0\varepsilon_{r,i})/\sigma_i$; i = core, shell) which were different by three orders of magnitude to simplify data analysis. Here, the material properties of the core were fixed at 0.1 mSm^{-1} for the conductivity (σ_{core}) and 2000 for the relative permittivity ($\varepsilon_{r,core}$). The shell's conductivity (σ_{shell}) was varied between 0.1 mSm^{-1} and 10 nSm^{-1} and its permittivity ($\varepsilon_{r,shell}$) varied from 10 to 2000. This set of material properties was selected as the spectra could usually be resolved for the frequency range discussed below and the range of shell properties could include those relevant for paraelectric shell regions in $BaTiO_3$[20] and insulating coatings for enhanced breakdown strength.[21]

For each combination of material properties, the impedance spectra were simulated from 1 Hz to 1 MHz. Initially a coarse frequency resolution was used with some enhanced resolution at the theoretical characteristic frequencies, $\omega_{max,}$ of the core and shell material ($\omega_{max} = 1/\tau$, the frequency where the magnitude of the value of the imaginary component of

impedance is greatest). Additional frequencies were simulated when visual inspection of the spectra revealed that minima or intercepts on the ordinates were poorly defined or missing.

Simulations were performed with COMSOL's ACDC package[22] using the electric currents module. First, the nested cube was built in COMSOL's geometry builder and material properties assigned to the core and shell regions. A Dirichlet boundary condition was used at the top and bottom of the model and an arbitrary potential difference of 1 V was applied. A Neumann condition set the current density to zero at the free surface of the model, confining the flow of current to inside the simulation geometry. Assuming that conductivity (σ) and relative permittivity (ε_r) are isotropic and time/frequency invariant allows the simulation to be performed only in the frequency domain, significantly reducing the computational burden. Assuming there is no induction, the potential (φ) can be solved using:

$$-\nabla.(\nabla\varphi(\sigma + j\omega\varepsilon_0\varepsilon_r)) = 0 \quad (1)$$

A tetrahedral mesh was used for space discretisation. The mesh size was set by a convergence study of the values obtained for each impedance formalism at 1 Hz and 1 MHz for four models (see supplementary data, **figures S2, S3** and **table S2**). An acceptable level of convergence was achieved with 0.47 million degrees of freedom when all the formalisms varied by ±1% or less. This mesh size was used throughout the study. As φ is a scalar quantity there is one degree of freedom per node.

3. Immittance Analysis

The dual resistor-capacitor (RC) circuit is a popular equivalent circuit for modelling ceramics with conductive grains and resistive grain boundaries. This is commonly referred to as the brick layer model following the work of Bauerle.[5] There is some debate regarding the validity of this circuit where conduction through the grain boundary parallel to the electric field is no longer negligible; as in nano-grained ceramics and some core-shell structures. Näfe[23] considered an additional parallel branch, in a 'so-called' parallel brick layer model,

which was successfully applied to nano-grained ceria by Hwang.[24] However, a multi-formalism analysis of the parallel variants of the brick layer model is lacking.

Here we consider two equivalent circuits. There are up to three components of the core-shell microstructure to be modeled: the core, the component of the shell perpendicular to the applied field and the component of the shell parallel to the applied field (if this is conductive enough to short-circuit the core). Each component is represented by a resistor and capacitor connected in parallel. The values of resistance and capacitance are calculated using:

$$R = \frac{l}{\sigma A} \tag{2}$$

$$C = \frac{\varepsilon_r \varepsilon_0 A}{l} \tag{3}$$

where ε_0 is the permittivity of free space, l is the length and A is the area of a given microstructural component. All values for geometric factor (A/l) together with a plan view of the SLM and encased model with all lengths and areas indicated are given in the supplementary material (see **figure S4** and **table S3**). Values for ε_r and σ are the same as those used in the FEM for the core and shell regions. Neglecting the contribution of the parallel shell gives a dual RC circuit (see **figure 1A**). If the parallel shell is considered, a triple RC circuit is required (see **figure 1B**).

Three different microstructural configurations were considered, giving three models to fit the immittance data simulated by FEM. The first is a series layer model (SLM), [18] which assumes that layers of core and shell material are stacked on top of each other perpendicular to the applied field as described in **figure 1C**. As the two layers are connected in series the current must flow homogeneously through them. Hence all the material contributes to the electrical response. The second is a series brick layer model (SBLM), which is an encased model where the shell is significantly more resistive than the core. We assume negligible current flows through the parallel component of the shell and hence this volume can be

neglected (see **figure 1D**). As before, current must flow homogeneously through all layers. The third is the parallel brick layer model (PBLM), which assumes significant current flows through the parallel component of the shell (see **figure 1E**). This requires an extra branch (see figure 1B) in the equivalent circuit. The geometries are shown in figure 1.

The immittance response of the two equivalent circuits was calculated for each combination of conductivity and permittivity chosen for the core and shell regions. Resistance and capacitance values were calculated using the geometric factors of the three models (see table S3) and the chosen conductivity and permittivity values. No refinements were made to the equivalent circuits, since they are compared to the FEM simulations with the same input parameters.

Immittance intercepts were acquired in all formalisms from both the more commonly used Nyquist plots of Z*, M* and also spectroscopic plots of the real part of the complex capacitance (Re(C*) = C'), the real part of the admittance (Re(Y*) = Y'), the imaginary part of the electric modulus (Im(M*) = M'') and the imaginary part of the impedance (Im(Z*) = Z''). Expressions for the immittance intercepts are shown in **figure 2** and their relations to the equivalent circuits in **table 1**. A collection of derivations of these equivalent circuits and their resulting immittance plots is given in ref. [25]

If a fit did not possess the same number of intercepts and minima as the FEM calculation, it was discarded. Otherwise, the magnitude of the difference between the FEM result and the fit result was calculated for each intercept or minimum observed. These differences were averaged over the total number of intercepts and minima to construct a metric of how well the fit replicated the FEM calculation. The fit with the lowest average difference was deemed optimal.

Resistance and capacitance values were extracted from the FEM calculation using the interpretations of intercepts and minima given in figure 2 and table 1. When there was more than one response present in a single formalism (e.g. well defined core and shell response or

two arcs in a Nyquist plot), the assignment of the response to the core or shell was based on consideration of the ω_{max} value with respect to the theoretical time constants of the core and the shell (τ_{core} and τ_{shell}, respectively). These were calculated using:

$$\tau_i = \frac{\varepsilon_0 \, \varepsilon_{r,i}}{\sigma_i}; i = core, shell \quad (4)$$

where ε_0 is the permittivity of free space and $\varepsilon_{r,i}$ is the relative permittivity of the core or shell. Since τ_i is inversely proportional to $\omega_{max,i}$ if $\tau_{core} < \tau_{shell}$ (i.e. $\omega_{max,core} > \omega_{max,shell}$) the core response should occur at a higher frequency than that of the shell (and vice versa).

Once assigned to core or shell, the resistance and capacitance values were converted into conductivity and permittivity values using the geometric factor of the optimal equivalent circuit for a given set of material properties. For the SLM and SBLM this could be done with the basic equations for resistance and capacitance. However, for the PBLM, core properties contain terms from the parallel shell (p-shell) contribution:

$$\sigma_{core} = \frac{1}{G_{core}}\left(\left(\frac{1}{R_{core}}\right) - \left(\sigma_{shell} G_{p-shell}\right)\right) \quad (5)$$

$$\varepsilon_{r,core} = \frac{1}{G_{core}\varepsilon_0}\left(C_{core} - \left(\varepsilon_0 \varepsilon_{r,shell} G_{p-shell}\right)\right) \quad (6)$$

where G_k is the geometric factor (area over length). The values for σ_{shell} and $\varepsilon_{r,shell}$ closest to the input values were used.

This was repeated for the resistance and capacitance values obtained from each formalism, when available. The magnitude of the difference between the input and extracted conductivity and permittivity values for each formalism was compared to determine which formalism was best for different combinations of material properties.

4. Results

4.1. Equivalent Circuit Evaluation

A wide range of material property combinations was simulated using FEM and compared to the three models. In all cases the shell material properties were varied and the core material properties fixed. Plots of the mean error for each model are given in **figure 3**.

The SLM usually gave the worst fit with errors of up to ±149% (see **figure 3A**); however, it performed better when the core and shell had very similar properties, giving errors of ±0.02% (see bottom left corner of figure 3A). Errors in the SLM fit rose to over ±10% when the shell properties were reduced by an order of magnitude relative to the core. There were three large regions where the SLM did not have the same number of immittance responses as the FEM data and hence was considered invalid (see white regions of figure 3A). These regions are found when either $\tau_{core} > 10\tau_{shell}$ or $\tau_{shell}/100 < \tau_{core} < \tau_{shell}/10$.

Except when the shell properties were similar to the core ($\varepsilon_{r,shell} > 500$, $\sigma_{shell} > 20$ μSm^{-1}), the SBLM gave smaller errors than the SLM (see **figure 3B**). Typically, the SBLM gave a larger error (maximum of ±14%) when the core had a similar conductivity or permittivity to the shell. A region of minimum error (±0.47%) centred on $\sigma_{shell} \sim 10$ μSm^{-1}, $\varepsilon_{r,shell}$ ~300. The PBLM fit usually showed the lowest error (see **figure 3C**). This was as low as ±0.02% when the shell and core properties were the same but increased to ±5% when the core and shell properties were very different. The PBLM performed better than the SBLM (by ±5% to ±10%) when either $\sigma_{shell} \sim \sigma_{core}$ or $\varepsilon_{r,shell} \sim \varepsilon_{r,core}$. This difference decreased as σ_{shell} or $\varepsilon_{r,shell}$ decreased.

A plot showing which model had the lowest fitting error is given in **figure 3D** and is divided into four regions (I-IV). The red dot in each region marks a data point where the immittance spectra are shown (in the main paper or the supplementary information). In region I, $\sigma_{shell} \sim \sigma_{core}$ and the PBLM performs the best. An example set of spectra is given in **figure 4 A,B** (red point; region I, figure 3D: $\sigma_{shell} = 0.1 mSm^{-1}$, $\varepsilon_{r,shell} = 100$) where the SLM gives a poor

fit to each of the spectra. The SLM also fails to produce a minimum in the M* Nyquist arcs (see figure 4 A). For the formalisms weighted towards capacitance (M*, *M''* and *C'*, figures 4A, **S5 C** and **E**, respectively) both the SBLM and PBLM agree with the FEM data. The SBLM over-estimates the low frequency resistance in the formalisms that are more sensitive to resistance (Z*, *Z''* and *Y'*, **figures S5B, D and F**).

The SBLM provides the best fit in region II but only ~1% better than the PBLM. While the SBLM and PBLM could be considered equally good at fitting the experimental data, the SBLM is still a superior choice as it requires fewer parameters than the PBLM. See the supplementary information and **figure S6A-F** for a detailed discussion of this region and the immittance spectra.

In region III, $\varepsilon_{r,shell} \sim \varepsilon_{r,core}$ and σ_{shell} becomes lower than σ_{core}. Example spectra are given in **figures 4C** and **D**, **S7A-F** (red point, region III, figure 3D: σ_{shell} = 0.1 μSm^{-1}, $\varepsilon_{r,shell}$ = 1000). The only significant differences between the PBLM and SBLM are visible in the M* Nyquist plot (figure 4C) and the *M''* Bode plot (figure S7 E), where the SBLM underestimates the total capacitance (recall the M* arc diameter is equal to inverse capacitance). There is one point where the computer program analysing the data chose the SLM in region III (see red cross, figure 3D, spectra not shown). This was an extreme case as both the PBLM and SBLM had a minimum in their Z* arcs whereas there was no minimum in the FEM data. However, visual inspection revealed that the SLM was a much poorer fit (overestimating all arc diameters by a significant margin). The closest fit was provided by the PBLM.

There is a mixture of areas in Region IV where either the PBLM or SBLM performs slightly better. The difference between the fits is typically less than 0.1%. We therefore recommend using the SBLM in this region. The small increase in quality of fit does not justify the extra parameters required for the parallel shell component of the PBLM. In this study, however, we will use the fit with the lowest error for the sake of consistency.

4.2. Conductivity and Permittivity Extraction

For each data point, values of σ_{shell}, $\varepsilon_{r,shell}$, σ_{core} and $\varepsilon_{r,core}$ were extracted using all available impedance intercepts (see figure 2) and the basic equations for resistance and capacitance. The geometric factors used to convert from resistance and capacitance to conductivity and permittivity values are derived from the geometries shown in figure 1. The smallest errors (i.e. those for the most accurate model) obtained when comparing the extracted properties to those originally input into the FEM are given in **figure 5**. This is achieved by using the geometric factor of the optimal model (see figure 3D) and best immittance formalism, detailed in section 4.3.

The absolute error in the extracted properties did not exceed ~±100% except for σ_{shell} (up to ±3000%). The region where the errors are greatest in both the extracted shell properties (**figure 5 A,B**) and the extracted core properties (**figure 5 C,D**) is centred about the line where $\log(\tau_{shell}/\tau_{core}) = 0$, i.e. $\tau_{shell} \sim \tau_{core}$. For shell properties this region extends to where the core and shell properties remain similar ($\sigma_{shell} > 0.01$ mSm^{-1}, $\varepsilon_{r,shell} > 100$) but narrows as $\varepsilon_{r,shell}$ falls and σ_{shell} rises, vanishing at $\sigma_{shell} \sim 3$ μSm^{-1}, $\varepsilon_{r,shell} \sim 30$. For core properties, the region of high error extends further than (and in the opposite direction to) that for shell properties, to $\sigma_{shell} < 0.01$ mSm^{-1}, $\varepsilon_{r,shell} < 30$. As $\varepsilon_{r,shell}$ rises and σ_{shell} falls, it narrows to a point ($\sigma_{shell} \sim 0.03$ mSm^{-1}, $\varepsilon_{r,shell} \sim 350$).

4.3. Choice of Immittance Formalism

The most successful formalism for extracting $\varepsilon_{r,core}$ values depends strongly on the values of σ_{shell} and $\varepsilon_{r,shell}$ being considered. This is summarised in **figure 6** using the notation of **table 2**. Similar plots for σ_{core}, σ_{shell} and $\varepsilon_{r,shell}$ are given in the supplementary data (see **figures S8-**

S10). Again, only regions where the intrinsic values can be extracted within ±25% of the known inputs are plotted. The most successful formalism is given first. If another formalism can extract the conductivity or permittivity values with an error of within ±10% of the first one, these are listed in brackets in order of increasing error. The shapes of the regions have been simplified to enhance intelligibility. The supplementary material gives the full order of preference and the error values for each formalism for all data points is given.

There are distinct regions where one formalism is superior to all others (including where it is the only usable formalism), as shown in figure 6. Conversely, there are regions where any formalism gives good results (regions marked ALL in the bottom left of figures 6 and S8; also on the line $\log(\tau_{shell}/\tau_{core}) = 2$ in figures S9 and S10). Bode plots of Im(M*) = *M''* and Im(Z*) = *Z''* often yield good results for all conductivity and permittivity values although examples are close to regions of high error (see figures 6 and S8-S10). Finally, where $\tau_{shell} > 1000\tau_{core}$, *Y'* and *C'* are best for extracting σ_{shell} and $\varepsilon_{r,shell}$ (see figures S9 and S10). When τ_{shell} is in the range $1000\ \tau_{core} > \tau_{shell} > 100\ \tau_{core}$, any formalism may be used except *Z'*. A much-simplified summary of these results is given in **figure 7**, which shows which immittance formalism is best for extracting conductivity and permittivity values from the core and shell for the models and parameters considered.

5. Discussion

Comparing the three fits revealed that the SLM was inappropriate for modelling the electrical response of core-shell microstructure unless the core and shell properties were similar (see figures 3, 4, S5-S7). Ruling out the SLM, several regions were identified where either the SBLM or PBLM was preferable depending on the shell properties (see figure 3D). In region I, where the core and shell had similar conductivity but the shell permittivity differed significantly, the PBLM gave the best fit to the FEM data. This agrees with the literature,[12]

when the conductivity of the core and shell are similar, a significant amount of current can flow through the parallel component of the shell. Evidence for this can be seen in the immittance spectra shown in figures 4 and S5. The plots sensitive to capacitance, figures 4A and S5A, C, E, show little difference between the SBLM and PBLM. However, in the plots sensitive to resistance (figure S5B, D, F) the SBLM overestimates the low frequency resistance. The presence of the parallel pathway in the PBLM is needed to reduce the resistance and fit the FEM data correctly when the core and shell conductivities are similar.

In region II the SBLM was marginally better than the PBLM (around 1%). Here the core and shell time constant was similar but the shell conductivity and permittivity are lower than the core. We expect a single merged response since $\tau_{shell} \sim \tau_{core}$. This was found in the Nyquist plots of M* and Z* (figure S6A, B) where differences between the SBLM and PBLM fits were greatest. The inset graphs show the PBLM underestimates the total resistance and overestimates the total capacitance. The lower value of σ_{shell} (0.01 mSm^{-1}) inhibits current flow through the parallel shell component. Since $\varepsilon_{r,shell} < \varepsilon_{r,core}$ (274) the contribution to the overall capacitance from the parallel shell is negligible. As the parallel pathway is not needed, the SBLM provides the best fit for the FEM data in region II. We emphasise that the SBLM is also superior to the PBLM because it requires fewer parameters.

The results for region III are surprising. As σ_{shell} is similar to or lower than in region II, the SBLM should be best here; however, the PBLM gives a better fit by up to ±10%. This is because the SBLM underestimates the high frequency capacitance (figure 4C). Since this was most obvious in the M* plot, we conclude that the parallel pathway must make a small contribution to the high frequency capacitance (M* is sensitive to small capacitances). As σ_{shell} is low there cannot be a large current flowing through the parallel part; however, the combination of $\sigma_{shell} \neq 0$ and $\varepsilon_{r,shell} \sim \varepsilon_{r,core}$ results in an increased contribution to the high frequency capacitance.

Additional simulations with the same material properties as those in figures 4C, D and S7 but varying the core volume fraction from 0.7 to 0.9 revealed that, as the shell became thinner, the error in the high frequency capacitance of the SBLM decreased (see **figure 8**). This was also the case for the PBLM but, given the steeper gradient of the SBLM line, the effect of the capacitance associated with the parallel shell becomes negligible when the core volume fraction is > 0.95. A similar effect was noted by Hwang et al.[26] who reported a parallel contribution from air gaps in a poor contact. Hence for core shell microstructures where both $\varepsilon_{r,shell} \sim \varepsilon_{r,core}$ and there is significant shell thickness, a parallel pathway in the equivalent circuit is needed.

Finally, in region IV there were places where either the SBLM or the PBLM performed better. Generally, the SBLM was better in regions adjacent to region II, implying a similar mechanism. However, typical differences between the PBLM and SBLM in region IV were less than ±0.1%. If material properties fall within this region, we recommend the SBLM be used. A gain of ±0.1% in accuracy does not justify the use of a more complex model.

The lowest errors for conversion of resistance and capacitance values from the spectra into conductivity and permittivity values for a 80:20 core:shell volume fraction model are plotted in figure 5. This gives the errors when using the optimal equivalent circuit and impedance formalism. The error for all extracted materials properties exceeds ±25% in a region centred on $\tau_{shell} \sim \tau_{core}$. For shell properties this region extends down to where $\sigma_{core} \sim \sigma_{shell}$ (bottom left corners of figure 5 A,B). For core properties, the high error region extends upwards to where the core and shell have very different properties (top right corner of figure 5 C,D). This difference in accuracy can be explained by considering the core volume fraction and the relative time constants of core and shell. If core and shell properties are similar, the core dominates the impedance response because the core volume fraction is so high. Hence extracting core properties from this region will give a minor error from differences in the geometric factor between the core and the whole encased model. It is curious that extraction

of the shell properties becomes more reliable (for the volume fraction studied) as shell properties become more different to the core although the time constants remain similar. This may be worth further investigation.

As the core and shell time constants become increasingly different the extraction of conductivity and permittivity values becomes more reliable. It is possible to extract reliable values when τ_{shell} and τ_{core} differ by two orders of magnitude - in good agreement with claims in the literature. Using the optimal equivalent circuit and impedance formalism a difference of only one order of magnitude is needed (see the sloping lines $\log(\tau_{shell}/\tau_{core}) = \pm 1$in figure 5).

Figures 6 and S8-S10 show several trends in which formalism(s) provided the most accurate extraction of conductivity and permittivity values. We recall (1) that only formalisms with less than ±25% error are shown and (2) that less successful formalisms are shown only if their accuracy is within ±10% of the optimal formalism. The figures illustrate that there are material property combinations where a formalism is either the only one that can extract anything or it offers at least 10% greater accuracy than any other. For example, an *M''* or *Z''* spectroscopic analysis can work well in regions surrounding the high error region in figure 6.

There are also regions where any formalism can be used, as the difference between them is negligible. This is true when $100\tau_{core} \sim \tau_{shell}$ and $\sigma_{shell} < 0.316$ μSm^{-1} (figures S9 and S10) and also for the bottom left corners of figures 6 and S8. When the shell is very resistive (<0.1 μSm^{-1}) the impedance spectra become less resolved and it may only be possible to extract shell properties using *Y'* or *C'* (see bottom right corner of figures S9 and S10). As the shell becomes less resistive (<0.5 μSm^{-1}) any formalism but Z* can be used. Z* fails since it depends on adequate low frequency data to resolve the low frequency real intercept.

A final significant observation is the interplay between *Z''* and *M''* spectra. These formalisms work well around the region of high error (figures 6, 7 and S8-S10). In regions where extracting both core and shell properties is possible with less than ±25% error, either *M''* spectra are best for the core and *Z''* spectra best for the shell or vice versa. These regions

can be found in figures 6 and S8-S10, centred on σ_{shell} ~ 0.05 mSm^{-1}, $\varepsilon_{r,shell}$ ~ 30 and σ_{shell} ~ 5 μSm^{-1}, $\varepsilon_{r,shell}$ ~ 300. This is in good agreement with experimental results,[15, 27] where combined *Z''* and *M''* spectroscopy has been employed to separate merged core and shell responses. It is useful to show this method can accurately extract conductivity or permittivity values if the correct equivalent circuit/microstructure geometry is assumed.

6. Conclusion

A multi-formalism comparison of the series layer model (SLM) and brick layer model with and without a parallel pathway to represent the parallel component of the shell (PBLM and SBLM, respectively) has been made with finite element simulations of a (80:20 core volume fraction) core-shell microstructure. The core conductivity and permittivity were fixed and values for the shell were varied. The values of shell material properties could be divided into four regions (see **figure 9**):

- Regions I and III had shell property values within half an order of magnitude of the core values. Here, a bricklayer model with a parallel pathway was required to model the impedance response.
- For region I the parallel pathway was required to fit the low frequency resistance (see figure 4B) due to the high level of current passing through the parallel component of the shell.
- For region III the parallel pathway was needed to fit the high frequency capacitance (see figure 4C) due to a significant contribution from the high permittivity of the shell.
- Regions II and IV had shell property values that were lower than the core's by at least half an order of magnitude. In this area either the SBLM provided a marginally better fit or the SBLM and PBLM were indistinguishable. Here the SBLM is recommended for its simplicity.

Examination of which immittance formalism could extract conductivity and permittivity values for the shell and core revealed distinct regions (see figures 6, 7 and S8-

S10) where different formalisms performed better. For some regions a particular formalism was clearly better for property extraction, for others, any formalism could be used (see figure 7). Complementary plots of the imaginary components of the impedance and electric modulus versus frequency were not only found to be a good method to deconvolute merged impedance spectra into the individual core and shell response (in good agreement with previous experimental work[15, 27]), but were also proved to be more accurate for extracting intrinsic properties by comparing to the known values input into the FEM code. Based upon the findings of this work, in good agreement with experimental studies[9, 10], some suggestions for fitting immittance data of materials are listed in the supplementary information.

Limitations on resources mean we can consider only a small number of material property combinations. However, they are sufficient to show optimal immittance formalisms for analysing data varies significantly with the input shell properties. Comparing known model inputs with extracted values demonstrates the necessity of analysing immittance data with multiple formalisms to probe all aspects of the electrical response. Future work should be undertaken to confirm whether this conclusion should be generalised to other core-shell microstructures such as those with realistic grain size distributions and compositional heterogeneity.

Supporting Information
Supporting Information is available from the Wiley Online Library or from the author.

Acknowledgements

We thank the Engineering and Physical Research Sciences Council for funding (EP/L017563/1 and EP/P015565/1).

Received: ((will be filled in by the editorial staff))
Revised: ((will be filled in by the editorial staff))
Published online: ((will be filled in by the editorial staff))

References

[1] A. Zeb and S. J. Milne, J. Mater. Sci.: Mater. Electron. **2017,** 26, 9243.

[2] X. Y. Huang and P. K. Jiang, Adv. Mater. **2015** 27, 546.

[3] R. G. Chaudhuri and S. Paria, Chem. Rev. **2012**, 112, 2373.

[4] M. B. Gawande, A. Goswami, T. Asefa, H. Z. Guo, A. V. Biradar, D. L. Peng, R. Zboril, and R. S. Varma, Chem. Soc. Rev. **2015**, 44, 7540.

[5] J. E. Bauerle, J. Phys. Chem. Solids, **1969**, 30, 2657.

[6] D. C. Sinclair, T. B. Adams, F. D. Morrison, and A. R. West, Appl. Phys. Lett. **2002**, 80 2153.

[7] S. B. Adler, Chem. Rev. **2004**, 104, 4791.

[8] X. G. Han, Y. H. Gong, K. Fu, X. F. He, G. T. Hitz, J. Q. Dai, A. Pearse, B. Y. Liu, H. Wang, G. Rublo, Y. F. Mo, V. Thangadurai, E. D. Wachsman, and L. B. Hu, Nat. Mater. **2017**, 16, 572.

[9] E. J. Abram, D. C. Sinclair, and A. R. West, J. Electroceram. **2003**, 10 165.

[10] A. R. West, D. C. Sinclair, and N. Hirose, J. Electroceram. **1997**, 1, 65.

[11] J. R. Macdonald, Impedance spectroscopy: emphasizing solid materials and systems, Willey-Blackwell, NY, USA, **1987**.

[12] N. J. Kidner, N. H. Perry, T. O. Mason, and E. J. Garboczi, J. Am. Ceram. **2008**, 91, 1733.

[13] D. P. Almond and C. R. Bowen, Phys. Rev. Lett., **2003**, 92, 157601.

[14] H. Kishi, Y. Mizuno, and H. Chazono, Jpn. J. Appl. Phys., Part 1, **2003**, 42, 1.

[15] D. C. Sinclair and A. R. West, J. Appl. Phys. (Melville, NY, U. S.), **1989**, 66, 3850.

[16] S. I. R. Costa, M. Li, J. R. Frade, and D. C. Sinclair, RSC Adv. **2013**, 3 7030.

[17] J. P. Heath, J. S. Dean, J. H. Harding, and D. C. Sinclair, J. Am. Ceram. Soc. **2015**, 98, 1925.

[18] J. C. Maxwell, A Treatise on Electricity and Magnetism, Cambridge University Press, Cambridge, UK **2010**.

[19] J. Fleig and J. Maier, J. Electroceram. **1997**, 1, 73.

[20] Z. Zhao, V. Buscaglia, M. Viviani, M. T. Buscaglia, L. Mitoseriu, A. Testino, M. Nygren, M. Johnsson, and P. Nanni, Phys. Rev. B. **2004**, 70, 024107.

[21] J. L. Qi, M. H. Cao, J. P. Heath, J. S. Dean, H. Hao, Z. H. Yao, Z. Y. Yu, and H. X. Liu, J. Mater. Chem. C. **2018**, 6, 9130.

[22] COMSOL Multiphysics®, AC/DC module. Stockholm, Sweden, 2018.

[23] H. Nafe, Solid State Ionics, **1984**, 13, 255.

[24] J. H. Hwang, D. S. McLachlan, and T. O. Mason, J. Electroceram. **1999**, 3, 7.

[25] J. P. Heath, Simulation of Impedance Spectroscopy in Electroceramics Using a Finite Element Method, PhD thesis, University of Sheffield, August, **2017**.

[26] J. H. Hwang, K. S. Kirkpatrick, T. O. Mason, and E. J. Garboczi, Solid State Ionics, **1997**, 98, 93.

[27] T. B. Adams, D. C. Sinclair, and A. R. West, Phys. Rev. B. **2006**, 73, 094124.

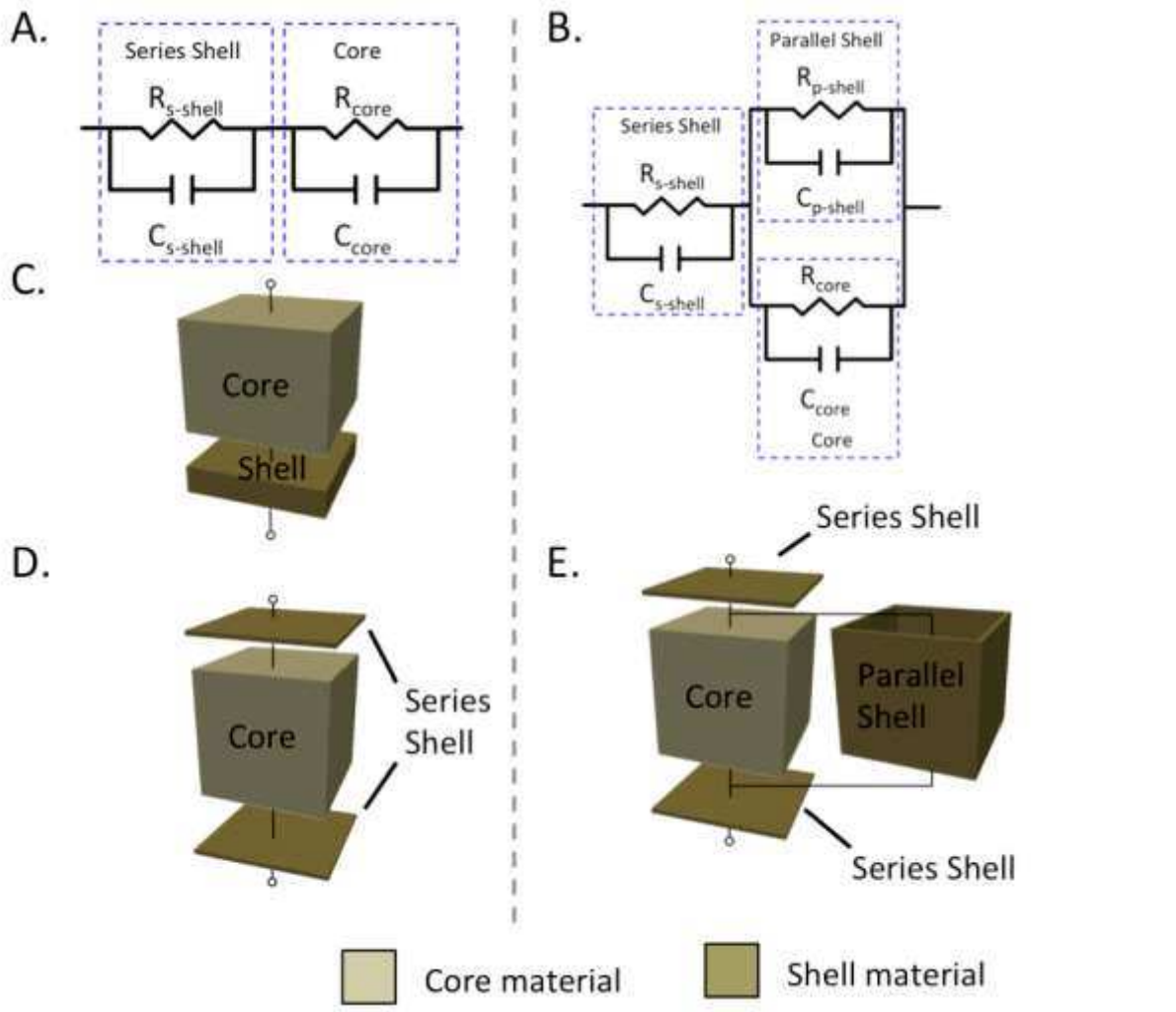

Figure 1. Schematics of the two equivalent circuits and the three corresponding geometries used to calculate RC values for the fits. (A) Dual RC circuit, (B) triple RC circuit with an extra branch for the parallel shell. (C) The series layer model, (D) the series brick layer model and (E) the parallel brick layer model. N.B. The 3D models are drawn to scale. (C) and (D) are used for circuit (A). (E) is used for circuit (B). The shell areas of models (C) and (D) are the same, however, since (D) neglects the presence of the parallel shell the overall shell thickness in (D) is less than (C). Therefore, despite both models using the same equivalent circuit (A), the SBLM's shell resistance is smaller and shell capacitance is greater than those of the SLM for the same core volume fraction. Hence there is a significant difference between using (C) and (D) to fit immittance spectra.

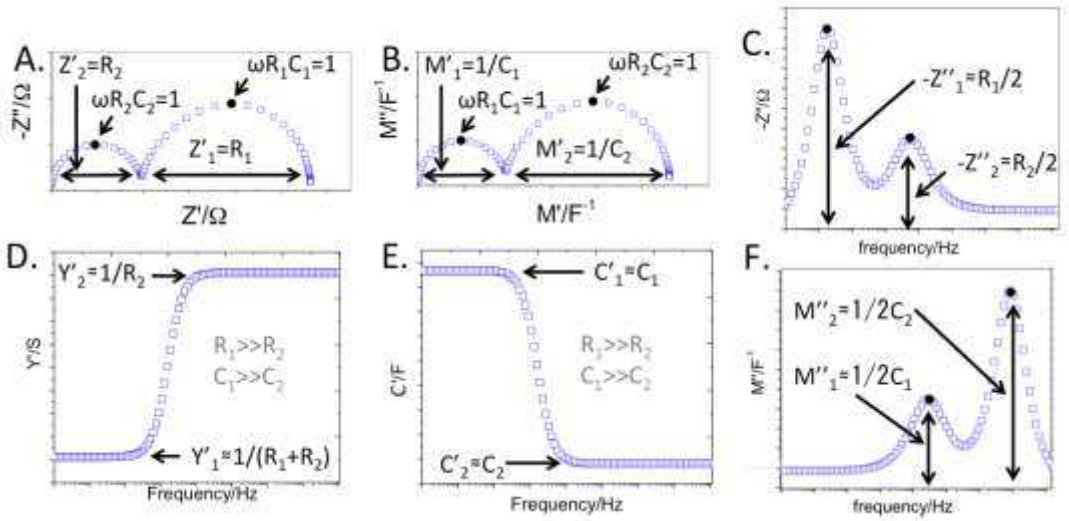

Figure 2. Schematics of the six immittance plots used in this work. (A) Nyquist plot of Z*; (B) Nyquist plot of M* and (C-F) Bode plots of Im(Z*), Re(Y*), Re(C*), and Im(M*), respectively. All plots assume dual RC elements connected in series (**figure 1A**) or a triple RC circuit in the configuration of **figure 1B** with a good separation of time constants and the core response at higher frequency than that of the shell. Poor separation of time constants leads to a single arc, peak or plateau. Subscript 1 indicates the low frequency response, subscript 2 the high frequency response.

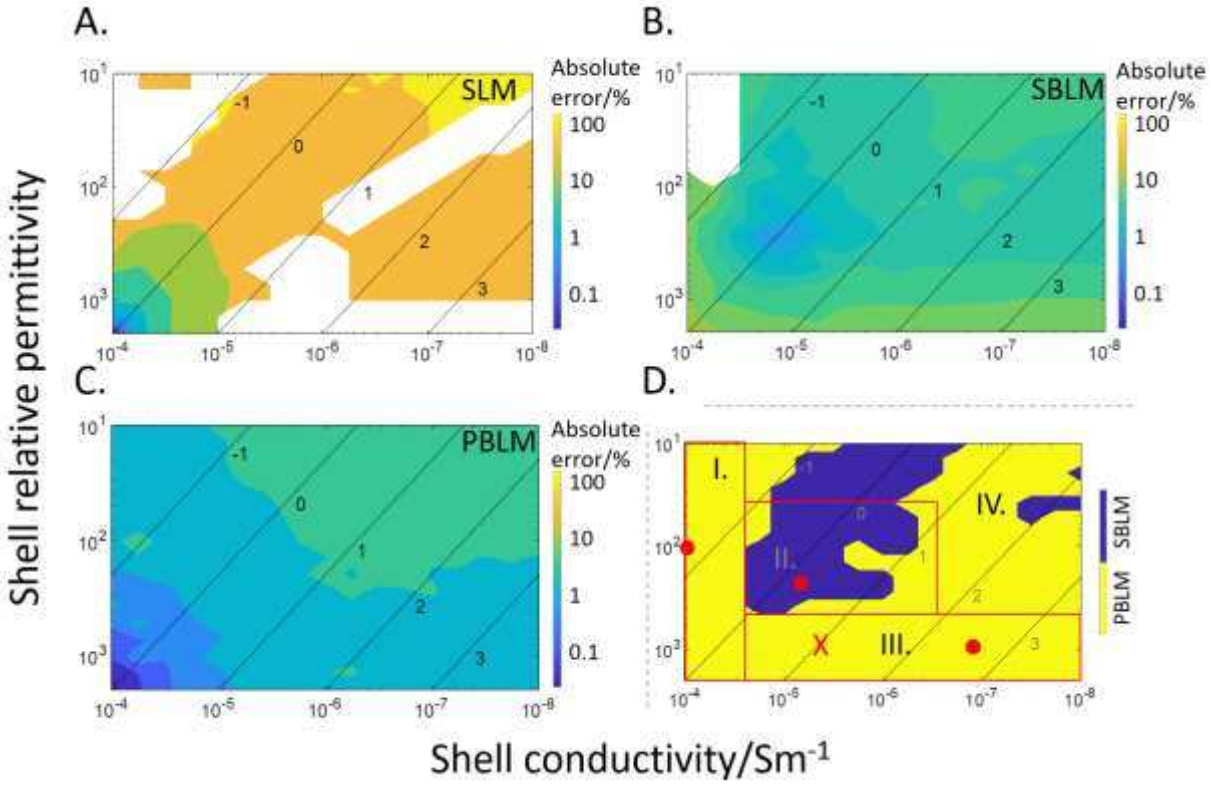

Figure 3. Contour plots of the absolute difference of the fits from the FEM results for (A) the SLM, (B) the SBLM and (C) the PBLM using logarithmic axes. White regions indicate the equivalent circuit was invalid (different number of immittance responses from the FEM results). (D) (Note different legend) shows where each fit has the lowest absolute difference. Red dots mark values where impedance data are shown in **figures 4 and S5-S7** are also discussed in the text. The red X indicates a fit that required visual inspection to find its impedance intercepts. The sloping lines show values of $\log(\tau_{shell}/\tau_{core})$.

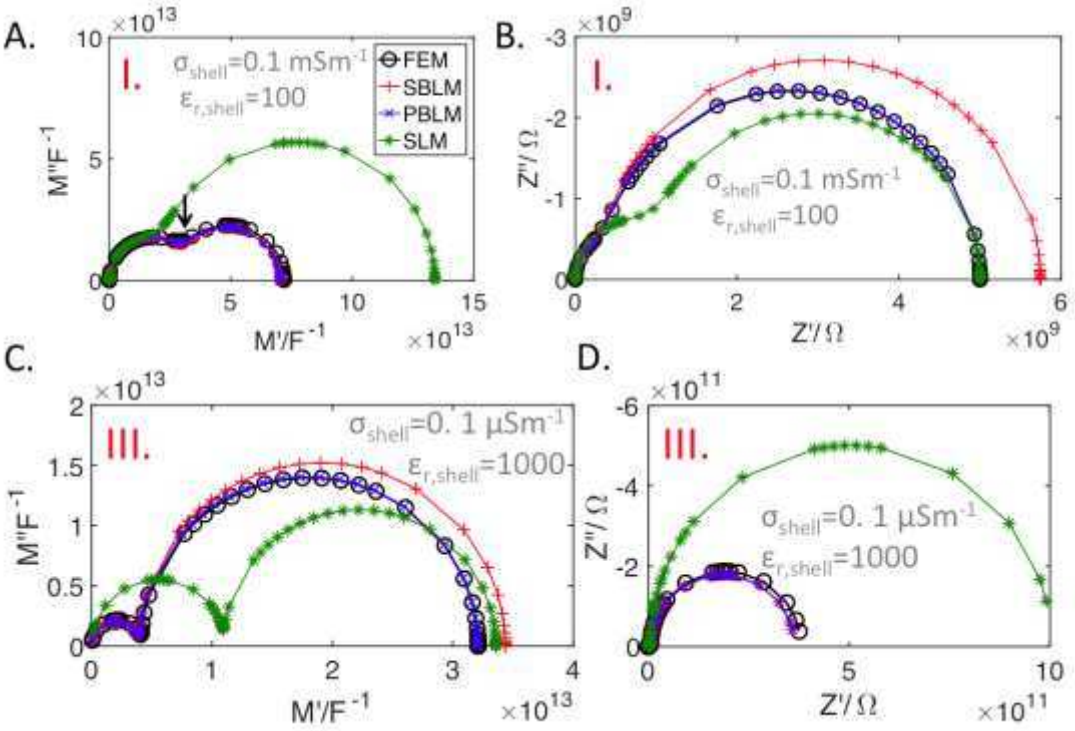

Figure 4. Comparison of the FEM simulated immittance response of the encased model with the three fits for the red points indicated in region I and III (**figure 3D**). The point considered is given in red text. The shell material properties used for the FEM are in grey text. (A, point I) Nyquist plot of the electric modulus, (B, point I) Nyquist plot of impedance, (C, point III) Nyquist plot of the electric modulus and (D, point III) Nyquist plot of impedance. The black arrow in (A) indicates the location of the minimum.

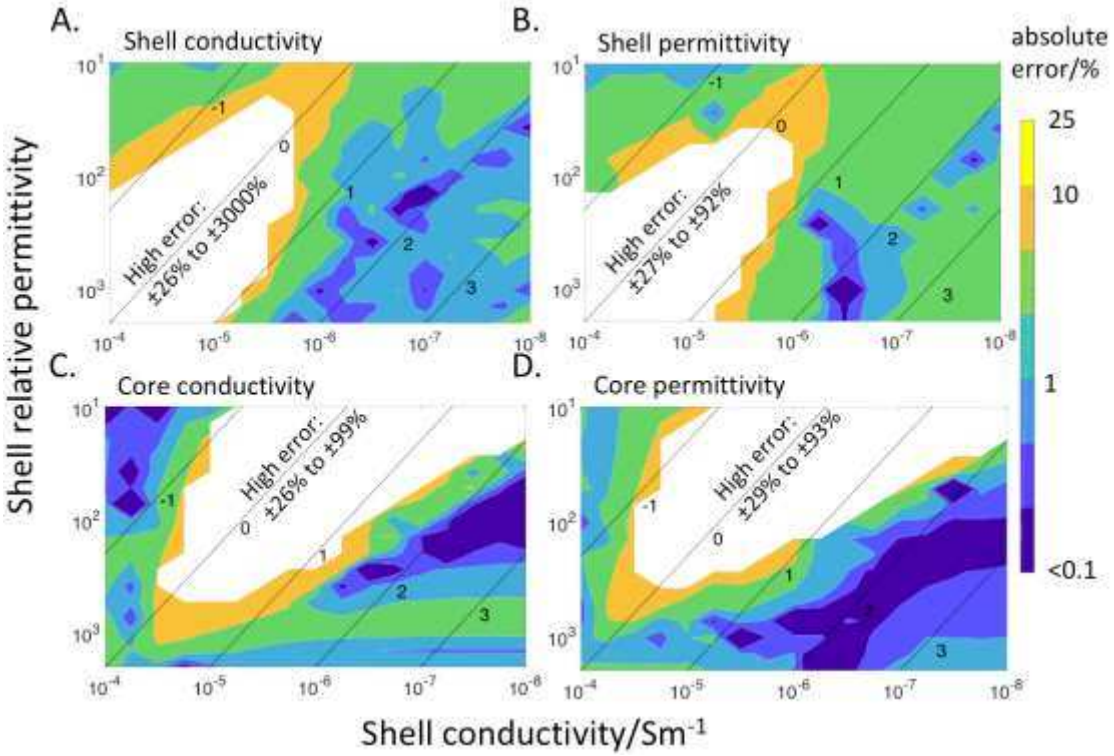

Figure 5. Absolute errors found in extracted material properties with respect to input values for (A) shell conductivity, (B) shell permittivity, (C) core conductivity and (D) core permittivity. All scales are logarithmic. Geometric factors for the optimal models are used throughout as described in figure 3D. The best immittance formalism for each data point is used as detailed in **figures 6 and S8-S10**. White regions have errors above ±25%. The sloping lines show values of $\log(\tau_{shell}/\tau_{core})$.

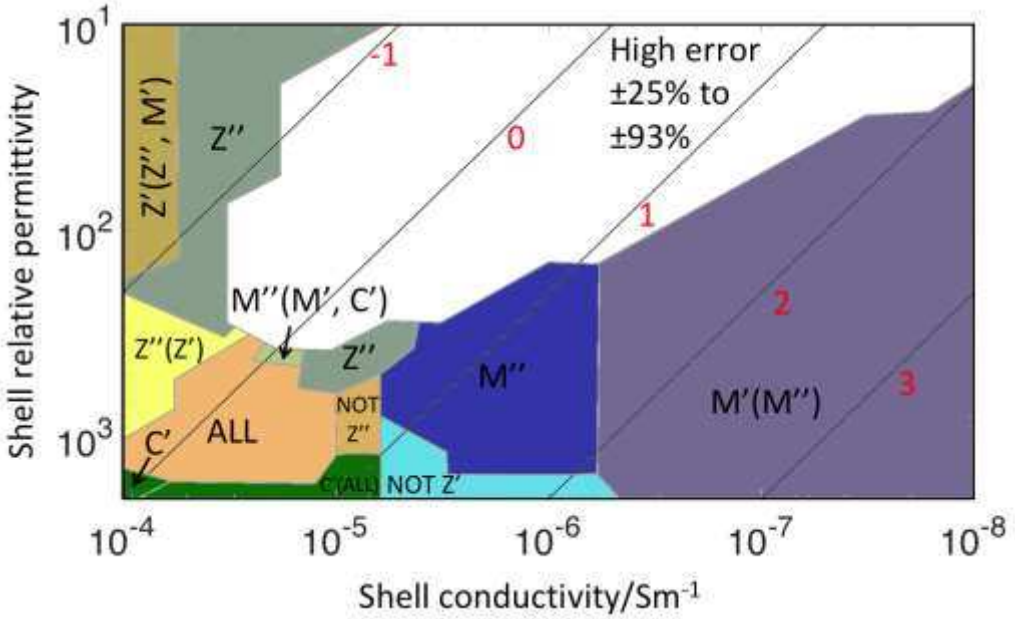

Figure 6. Optimal immittance formalisms for extracting the core permittivity. Only formalisms that give less than ±25% error are plotted. Regions with higher error are left blank. The best formalism is listed first. Any other formalisms within ±10% of the best are listed in brackets. ALL indicates that all formalisms used gave similar error, NOT indicates all but the listed formalism are effective. The shorthand for the various impedance formalisms is listed in **table 2**. The sloping lines show values of $\log(\tau_{shell}/\tau_{core})$. Different colour shading indicates a different formalism is optimal.

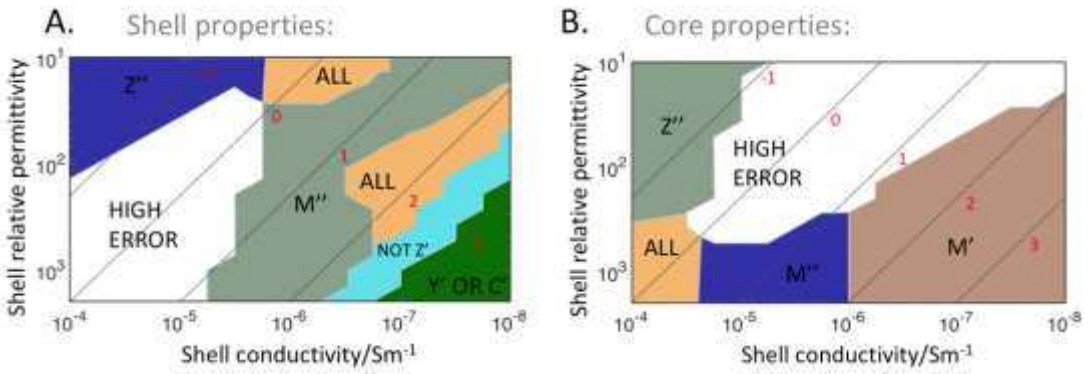

Figure 7**.** Schematic summarising formalisms recommended to be used when extracting (A) shell or (B) core properties. This figure consolidates figures 6 and S4-S6 and is further simplified for clarity.

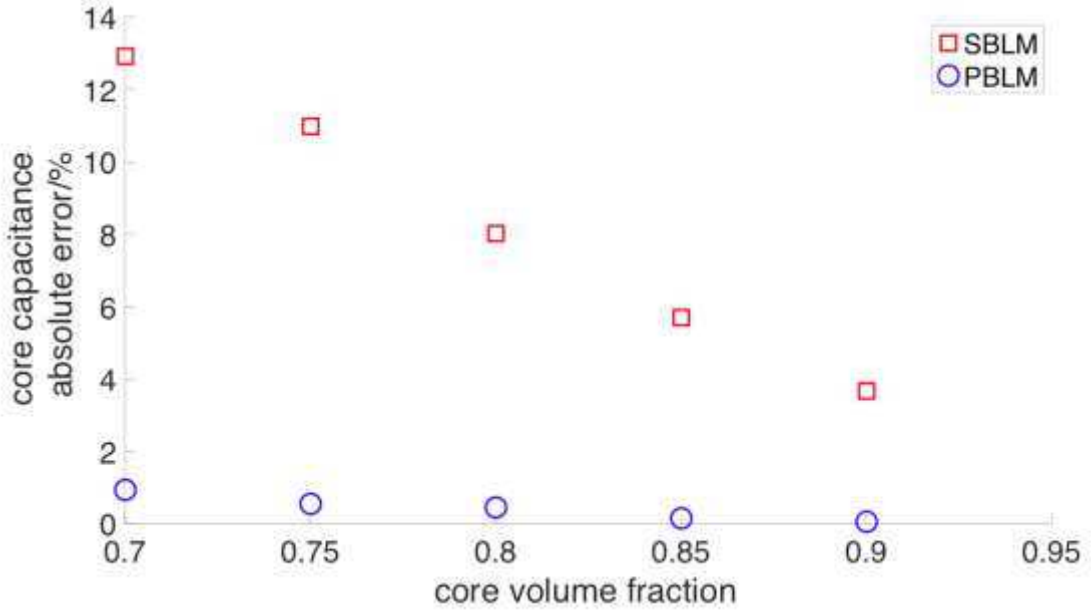

Figure 8. Plot of the absolute error (%) in the high frequency capacitance values predicted by the SBLM and PBLM compared to the FEM data as a function of core volume fraction.

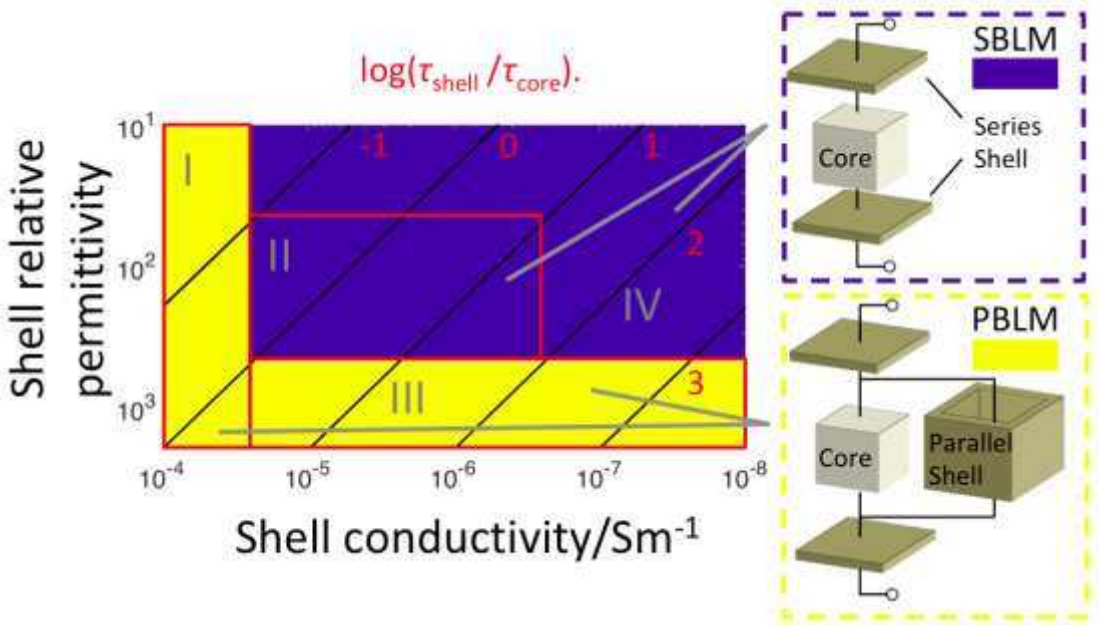

Figure 9. Schematic summarising where the different equivalent circuits should be used in the four regions discussed in the text for an 80:20 core-shell volume fraction microstructure. The sloping lines show $\log(\tau_{shell}/\tau_{core})$ values (red text).

Table 1. Physical meaning of the various impedance intercepts and plateaus with respect to the three equivalent circuits. Subscript s-shell, p-shell and core refer to the series shell, parallel shell and core components, respectively.

Intercept/Plateau	Relation to:	
	Dual RC	Triple RC
R_1	$R_{s\text{-shell}}$	$R_{s\text{-shell}}$
C_1	$C_{s\text{-shell}}$	$C_{s\text{-shell}}$
R_2	R_{core}	$1/(R_{core}^{-1} + R_{p\text{-shell}}^{-1})$
C_2	C_{core}	$(C_{core} + C_{p\text{-shell}})$

Table 2. List of shorthand notations for the formalisms used to extract conductivity and permittivity values. The type of data used to extract resistance and capacitance values is also given.

Intercept shorthand	Context	
	Conductivity	Permittivity
Z'	Resistance from Z* Nyquist arc diameter.	Capacitance as a function of Z* Nyquist arc diameter and ω_{max} ($C=1/\omega R$).
Z''	Approximate Z* arc diameter from Z'' Bode maximum ($R \approx 2Z''$).	Capacitance from substitution of ($R \approx 2Z''$) into ($C=1/\omega R$).
M'	Resistance as a function of M* Nyquist arc diameter and ω_{max} ($R=1/\omega C$).	Capacitance from inverse of M* Nyquist arc diameter.
M''	Resistance from substitution of ($C \approx 1/2M''$) into ($R=1/\omega C$).	Approximate M* arc diameter from M'' Bode maximum ($C \approx 1/2M''$).
Y'	Resistance approximated from Y' plateaus.	n/a
C'	n/a	Capacitance approximated form C' plateaus.

Impeadance spectra of core-shell microstructures of fixed core volume fraction are simulated with finite element modeling and analyzed in four formalisms. It is shown that the best formalism to study core-shell impedance spectra varies with shell conductivity and permittivty. The applicability of a brick layer model with a parallel pathway is also evaluated in four formalsims.

Impedance

James P. Heath, John H. Harding, Derek C. Sinclair, and Julian S. Dean*

The analysis of Impedance Spectra for Core-Shell Microstructures: Why a multi-formalism approach is essential

ToC figure

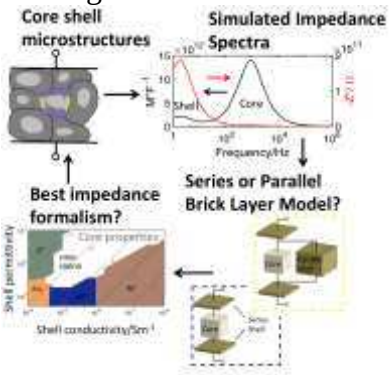

Supporting Information

The analysis of Impedance Spectra for Core-Shell Microstructures: Why a multi-formalism approach is essential: supplementary information.

James Heath, John Harding, Derek Sinclair, and Julian Dean*

Immittance formalisms:

Table S1. The four complex immittance formalisms, their relation to Z* and their sensitivities. M* and C* are given here in the absolute form; sometimes these are presented with the $j\omega$ term multiplied by C_0, where j is the square root of minus one, ω is the angular frequency and C_0 is the vacuum capacitance of the measured cell.

Formalism	Relation to Z*	Sensitive to:
Z*	---	Large resistances
Y*	$(Z^*)^{-1}$	Small resistances
C*	$(j\omega Z^*)^{-1}$	Large capacitances
M*	$j\omega Z^*$	Small capacitances

Model geometry (part 1):

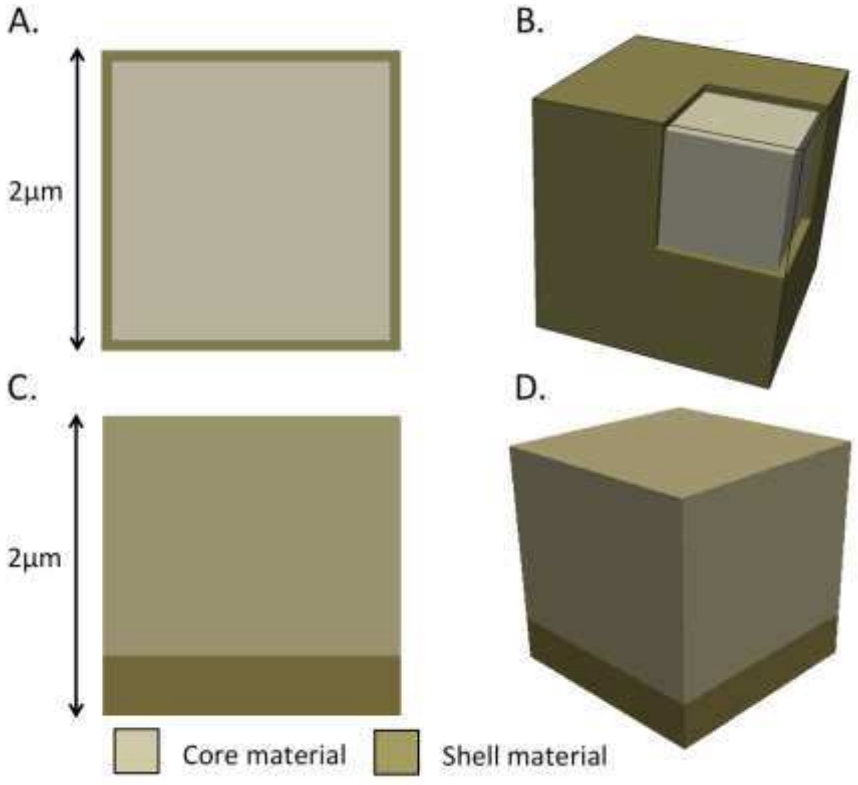

Figure S1. Geometry of the encased model and series layer model. (A) Cross-section of the encased model, (B) 3D encased model with a corner of the shell removed to show the core within; (C) cross section of the series layer model and (D) 3D series layer model.

Convergence study:

A convergence study was conducted to check that the meshing used in this study was appropriate. Four models with different material properties were chosen to give extreme combinations of shell permittivity and conductivity (see **table S2**). For each model the mesh division length was varied to give a range of degrees of freedom (a finer mesh gives more degrees of freedom) from 26266 to 940,000. Each simulation was carried out at 1Hz and 1 MHz as this range was used in the study. Outside this frequency range the numerical noise became unacceptably large. Ideally the whole frequency spectrum would be simulated but this would take impractically long for the finer meshes.

Table S2. List of material properties used in convergence study.

Model	σ_{shell} /Sm^{-1}	$\varepsilon_{r\text{-}shell}$
A	1.00e-8	10
B	1.00e-8	2000
C	1.00e-4	10
D	1.00e-4	2000

The value of the impedance was simulated at high and low frequency for all models and split into the real and imaginary parts. This was then converted into the real admittance (*Y'* = Re(Y*)), the real part of the complex capacitance (*C'*=Re(C*)), the real electric modulus (*M'*=Re(M*)) and the imaginary electric modulus (*M''*=Im(M*)). For each model and formalism the values over a range of mesh sizes were normalised to the largest value and are presented in **figures. S2 and S3** (low and high frequency, respectively). It can be seen there is less than ±1% variation with the degrees of freedom for all models. For the rest of the study a compromise of 470,000 degrees of freedom was deemed adequate.

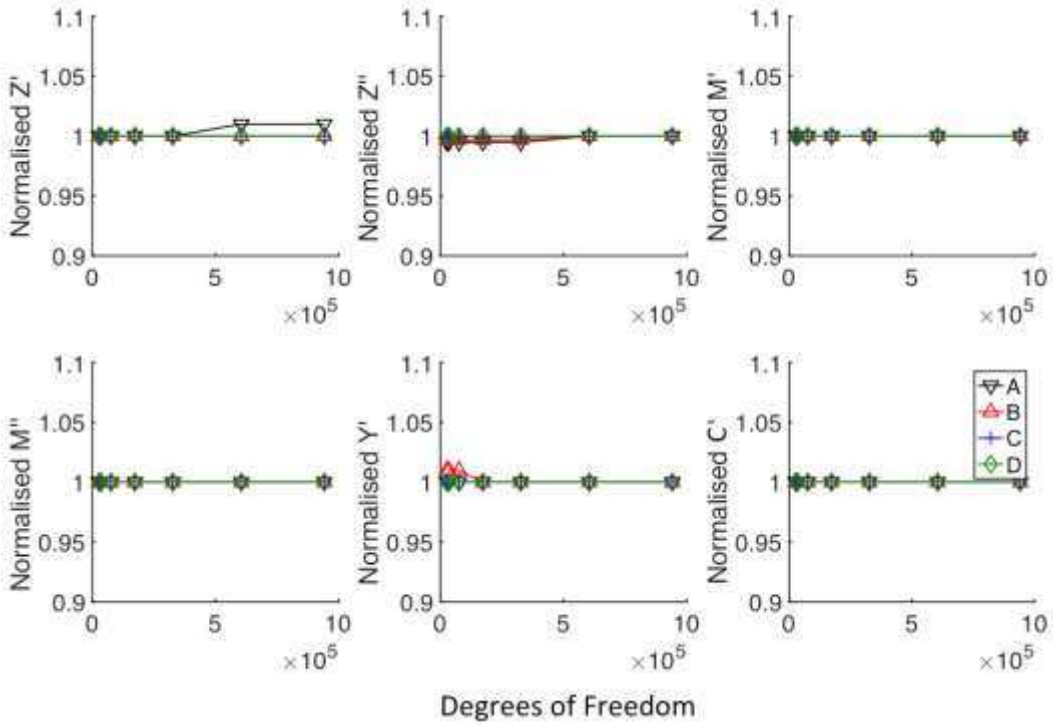

Figure. S2. Low frequency convergence. The legend refers to models A-D.

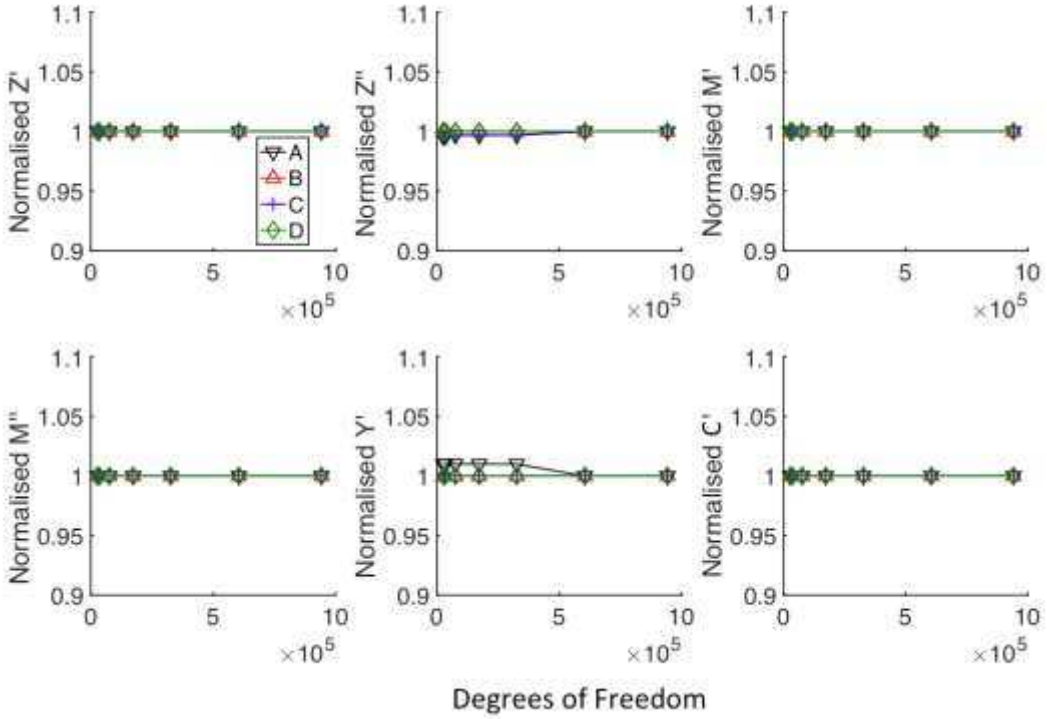

Figure. S3. Low frequency convergence. The legend refers to models A-D.

Model geometry (part 2):

The geometric factors are derived from the lengths and areas of the SLM and encased models (defined in **figure. S4**) and are listed in **table S3**.

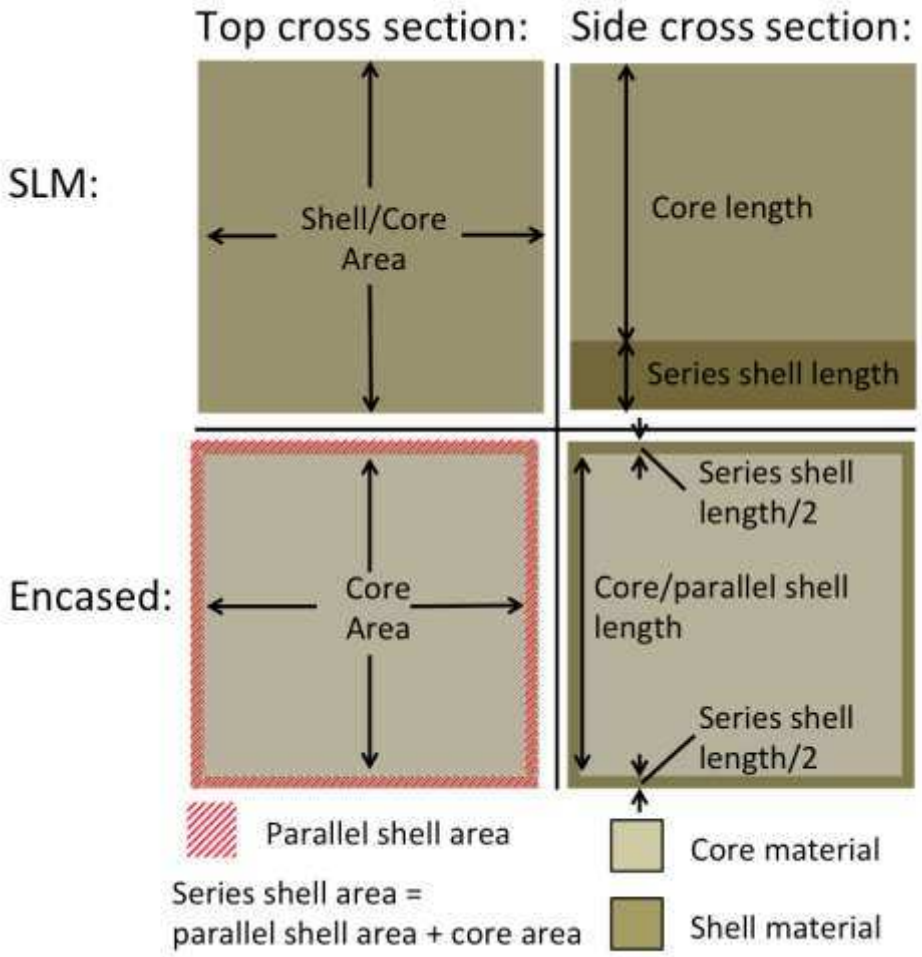

Figure S4. Plan view of the SLM and encased model showing where the lengths and areas in **table S3** refer to. Note the cross-sections bisect the models through their centres.

Table. S3. Lengths and areas assumed for the geometries of the three models and the resulting volumes/geometric factors of core and shell material.

Microstructure	Layer	Encased	
Quantity	SLM	SBLM	PBLM
Series shell length/μm	0.400	0.143	0.143
Series shell area/μm^2	4.000	4.000	4.000
Core length/μm	1.600	1.857	1.857
Core area/μm^2	4.000	3.447	3.447
Parallel shell length/μm	n/a	n/a	1.857
Parallel shell area/ μm^2	n/a	n/a	0.553
Core volume/μm^3	6.400	6.400	6.400
Shell volume/μm^3	1.600	0.572	1.600
Series shell geometric factor/μm	10.00	27.97	27.97
Core geometric factor /μm	2.500	1.857	1.857
Parallel shell geometric factor/μm	n/a	n/a	0.297

Immittance spectra:

Here the immittance spectra for the three points (I-III, defined in **figure 3D**) discussed in the text are given in all four formalisms (see **figures. S5, S6 and S7**). Note for the convenience of the reader the Nyquist plots of Z* and M* for points I and III have been repeated and are identical to those in the main text.

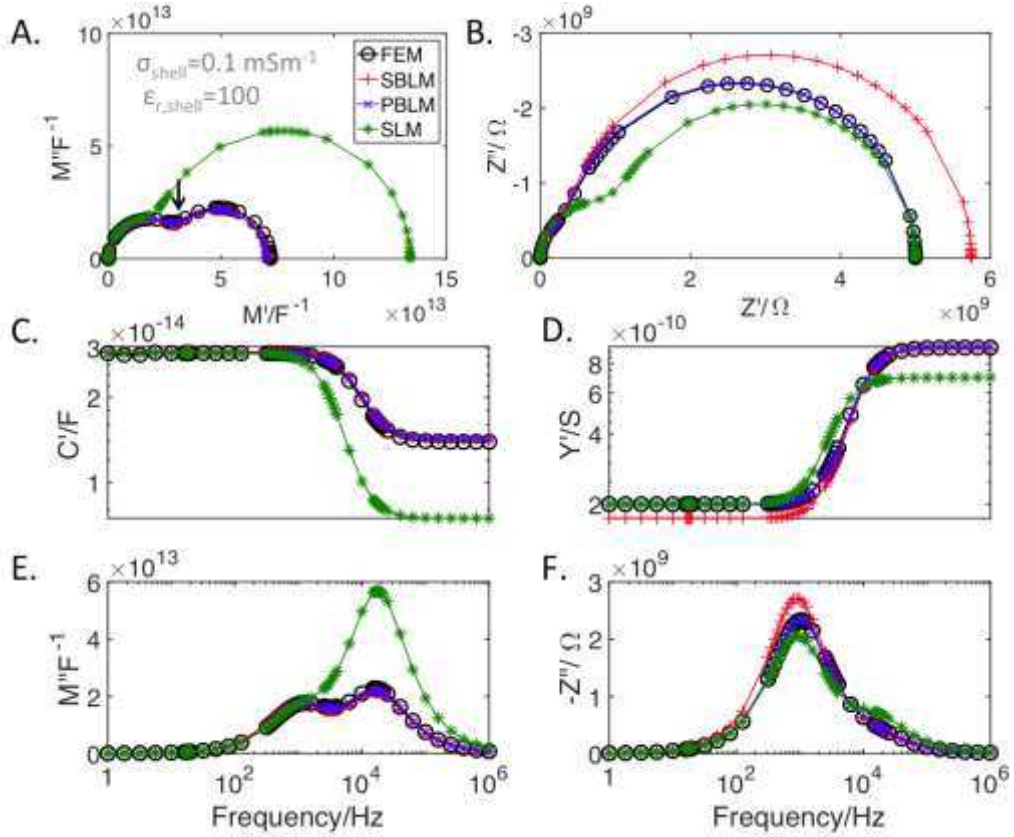

Figure S5. Comparison of the FEM simulated immittance response of the encased model with the three fits for the red point indicated in region I (**figure 3D**). The shell material properties used for the FEM are in grey text. (A) Nyquist plot of the electric modulus, (B) Nyquist plot of impedance, (C-F) spectroscopic plots of Re(C*), Re(Y*), Im(M*) and Im(Z*), respectively. The black arrow in (A) indicates the location of the minimum.

The spectra for the point which gives the largest (~1%) improvement in region II are shown in **figure S6** (red point, **figure 3D**: σ_{shell}=0.01 mSm^{-1}, $\varepsilon_{r,shell}$=274). The inset graphs in **figure S6A, B** highlight the better fit. The PBLM overestimates the total capacitance of the encased model and underestimates the total resistance.

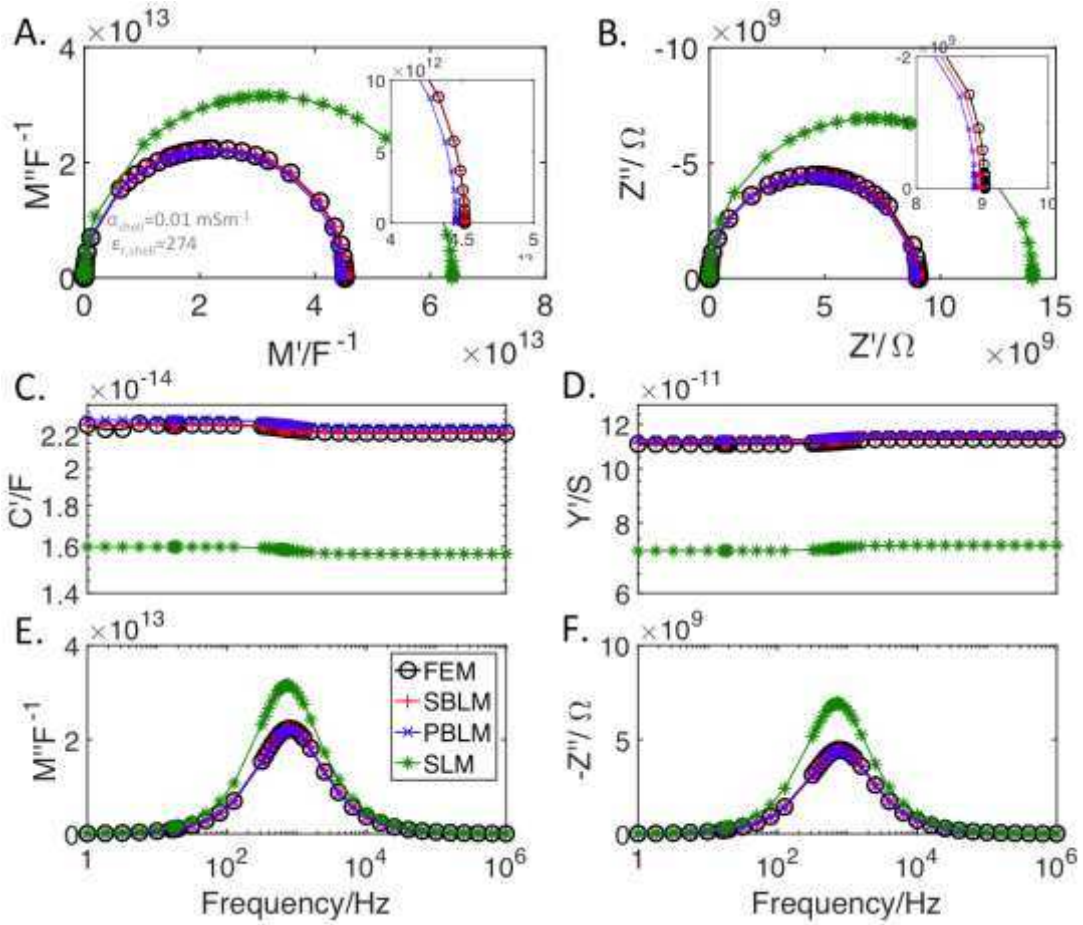

Figure S6. Comparison of the FEM simulated immittance response of the encased model for the red point indicated in region II (figure 3D). Input shell material properties are in grey text. (A) Nyquist plot of the electric modulus, (B) Nyquist plot of impedance, (C-F) spectroscopic plots of Re(C*), Re(Y*), Im(M*) and Im(Z*), respectively. The inserts in (A and B) show an enlargement of the rightmost x-axis intercepts excluding the SLM (green line).

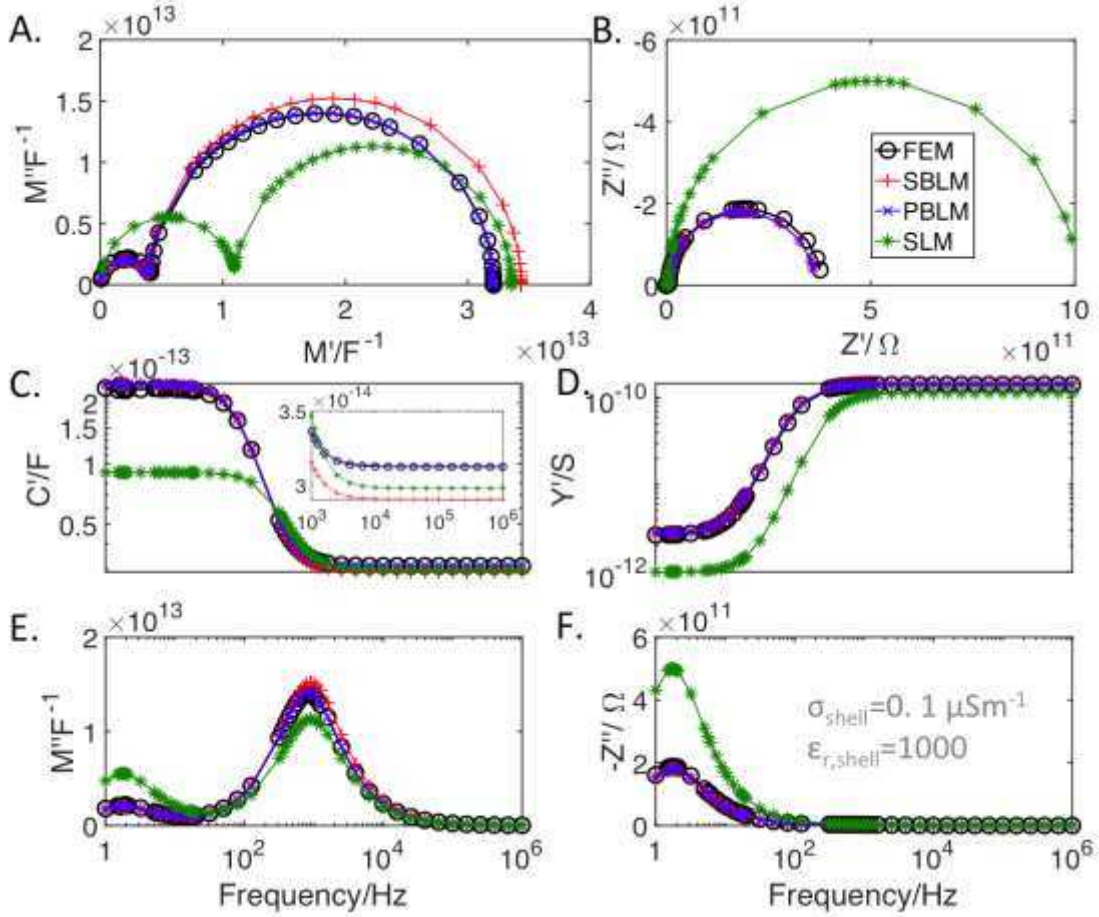

Figure S7. Comparison of the FEM simulated immittance response of the encased model for the red point indicated in region III (figure 3D) with the three fits. Input shell material properties are in grey text. (A) Nyquist plot of the electric modulus, (B) Nyquist plot of impedance, (C-F) spectroscopic plots of Re(C*), Re(Y*), Im(M*) and Im(Z*), respectively. Note the inset graph in (C) shows the high frequency data for Re(C*).

Immittance formalism maps:

Figures S8-S10 map which immittance formalisms extracted the core conductivity, shell conductivity and shell permittivity, respectively most accurately with respect to the values inputted into the FEM. Only formalisms that could extract the shell conductivity with less than ±25% error were plotted, regions with higher error are left blank. The best formalism is listed first. If there are any other formalisms that are within ±10% of the best formalism, these are listed in brackets in order of increasing absolute error. ALL indicates that all formalisms used gave similar error, NOT indicates all but the listed formalism are effective. The shorthand for the various impedance formalisms is listed in **table 2** (main text). The raw data used to construct these maps is available as a separate excel sheet that can be downloaded with this supplementary data.

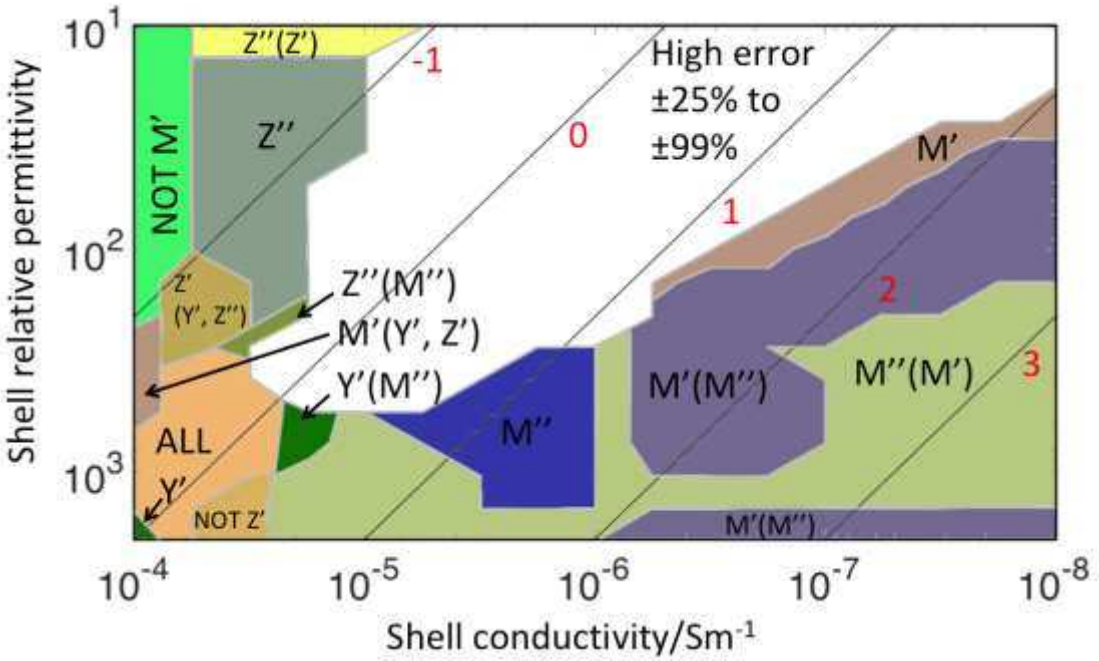

Figure S8. Plot mapping the optimal immittance formalisms for the extraction of the core conductivity. The sloping lines show log(τ_{shell}/τ_{core}) values (red text). Different colour shading indicates a different formalism is optimal.

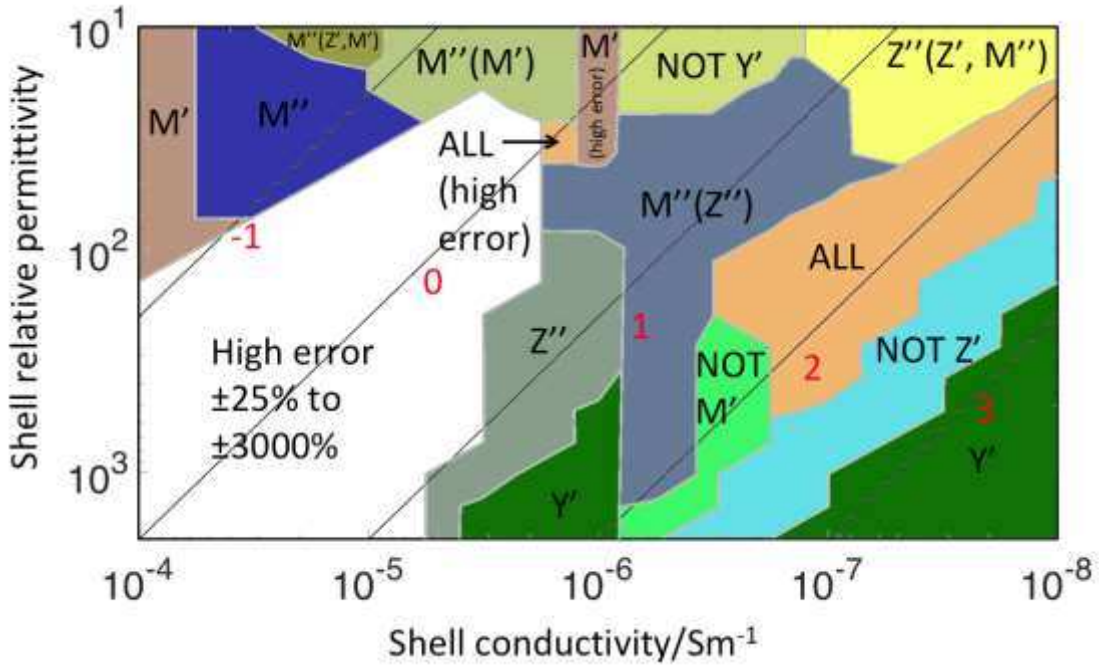

Figure S9. Plot mapping the optimal immittance formalisms for the extraction of the shell conductivity. All annotations are in the style of figure S8.

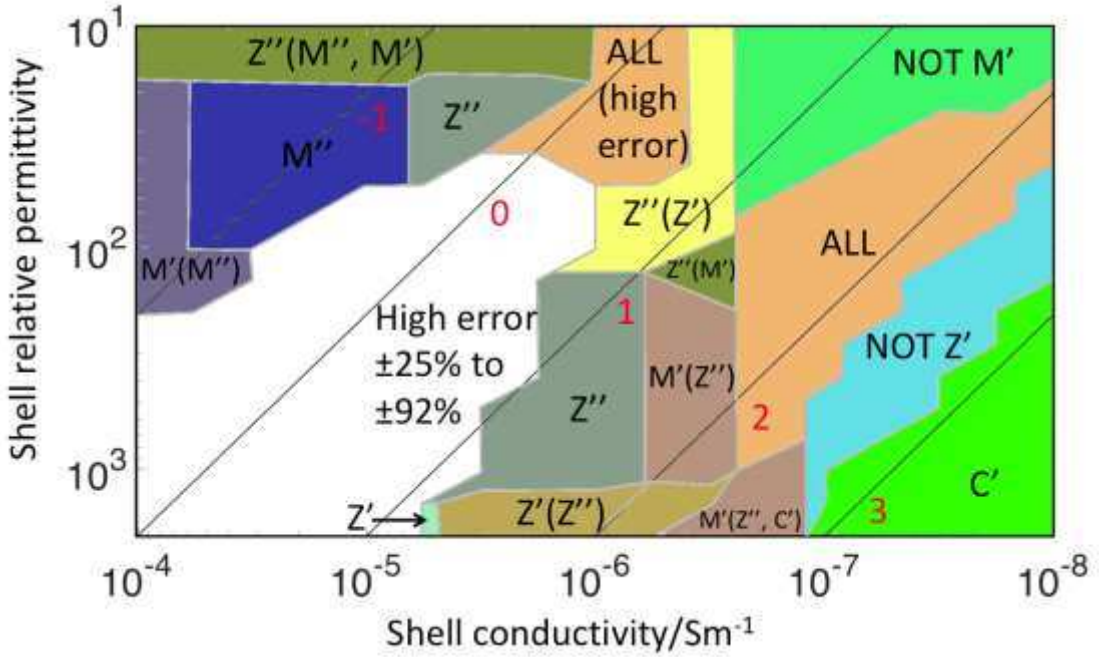

Figure S10. Plot mapping the optimal immittance formalisms for the extraction of the shell permittivity. All annotations are in the style of figure S8.

Suggestions for practitioners:

- Equivalent circuits should be constructed from circuit elements that have physical basis with respect to electrical microstructure and processes occurring within the sample.
- The equivalent circuit fits should be compared to the experimental data in two or more immittance formalisms over the entire measured frequency range. A good fit will work in all conditions.
- Parallel pathways may need to be considered for equivalent circuits fitting if the pathways are relatively conductive or contain high permittivity material.
- If Nyquist arcs of Z* and M* are incomplete at low frequency and fitting semi circles is impractical (e.g. distorted arcs), plateaus of *C'* and *Y'* Bode plots may provide better approximations of capacitances and resistances, respectively.
- When using combined *Z''* and *M''* Bode plots, if the frequency of the maxima of both peaks is significantly different, the measured sample is electrically heterogeneous. In the context of core-shell microstructures, one response may be due to the core and the other to the shell.
- When assigning the responses to different aspects of the microstructure consider the sensitivity of a formalism where the response is found. If there is only one response in Z* but two in M* it is likely one from M* has a low capacitance and is relatively conductive given the sensitivities of M* and Z* (see table S1).
- The temperature dependence of extracted conductivity and permittivity values should obey physical laws, for example the Arrhenius law for conductivity and the Curie-Weiss law for permittivity above the Curie Temperature where appropriate, e.g. ferroelectric materials.